A Forked Microvascular Phantom for Ultrasound Localization Microscopy Investigations

Hanyue Shangguan, *Graduate Student Member, IEEE*, Billy Y. S. Yiu, *Member, IEEE*, Adrian J. Y. Chee, *Member, IEEE*, and Alfred C. H. Yu, *Fellow, IEEE*

***Abstract*—In the development of ultrasound localization microscopy (ULM) methods, appropriate test beds are needed to facilitate algorithmic performance calibration. Here, we present the design of a new ULM-compatible microvascular phantom with a forked, V-shaped wall-less flow channel pair (250 μm channel width) that is bifurcated at a separation rate of 50 μm/mm. The lumen core was fabricated using additive manufacturing, and it was molded within a polyvinyl alcohol (PVA) tissue-mimicking slab using the lost-core casting method. Measured using optical microscopy, the lumen core's flow channel width was found to be 252 ± 15 μm with a regression-derived flow channel separation gradient of 50.89 μm/mm. The new phantom's applicability in ULM performance analysis was demonstrated by feeding microbubble (MB) contrast flow (1.67 to 167 μL/s flow rates) through the phantom's inlet and generating ULM images with a previously reported method. Results showed that, with longer acquisition times (10 s or longer), ULM image quality was expectedly improved, and the variance of ULM-derived flow channel measurements was reduced. Also, at axial depths near the lumen's bifurcation point, the current ULM algorithm showed difficulty in properly discerning between the two flow channels because of the narrow channel-to-channel separation distance. Overall, the new phantom serves well as a calibration tool to test the performance of ULM methods in resolving small vasculature.**

***Index Terms*— Additive manufacturing, forked lumen, microvascular phantom, ultrasound localization microscopy (ULM).**

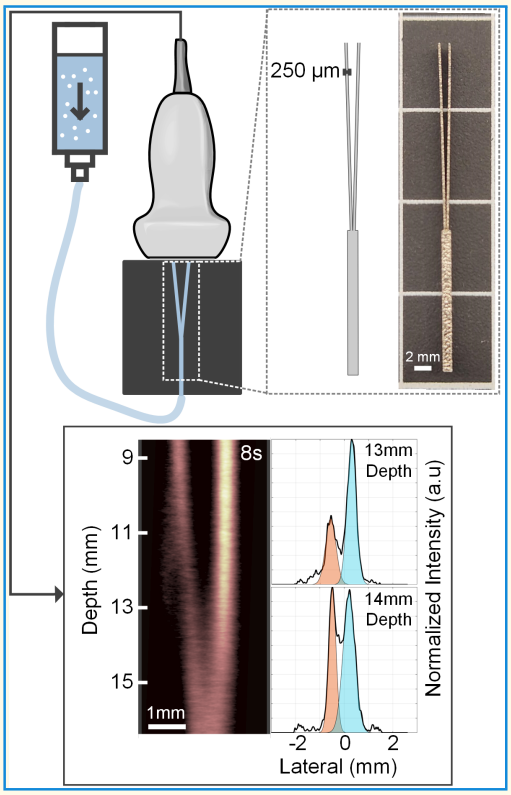

I. Introduction

ULTRASOUND localization microscopy (ULM) is a super-resolution imaging technique based on contrast echo localization [1], where the accumulated image of spatially isolated microbubble (MB) contrast signals over multiple frames enables the resolution of vascular features smaller than the diffraction limit. This technique facilitates the visualization of complex sub-millimeter scale vascular features [2], [3] and may provide velocity information within these features [4], [5]. Visualization of microvessels is after all important because it may provide insight on pathologies such as cancer and atherosclerosis [6], [7]. It may specifically help to elucidate microvascular development during disease progression, and it opens the possibility of tracking treatment response via vessel recession [7], [8], [9]. Microvascular imaging of human subjects has also shown experimental success for breast cancer and lower limb vascular visualization [4], [11]. Nevertheless, in humans, ULM image quality is known to be affected by various parameters including contrast delivery concentration [12], [13] and contrast agent selection [14], [15].

Manuscript received 8 May 2024; accepted 31 May 2024. Date of publication 4 June 2024; date of current version 15 July 2024. This work was supported in part by the Natural Sciences and Engineering Council of Canada under Grant CREATE-528202-2019 and Grant RPGIN-2022-04157, in part by E. W. R. Steacie Memorial Fellowship under Grant SMFSU-556263-2021, and in part by the National Institutes of Health under Grant R01EY028550. *(Corresponding author: Alfred C. H. Yu.)*

Hanyue Shangguan, Adrian J. Y. Chee, and Alfred C. H. Yu are with Schlegel Research Institute for Aging and the Department of Electrical and Computer Engineering, University of Waterloo, Waterloo, ON N2L 3G1, Canada (e-mail: alfred.yu@uwaterloo.ca).

Billy Y. S. Yiu was with Schlegel Research Institute for Aging and the Department of Electrical and Computer Engineering, University of Waterloo, Waterloo, ON N2L 3G1, Canada. He is now with the Department of Health Technology, Technical University of Denmark, 2800 Kongens Lyngby, Denmark.

Digital Object Identifier 10.1109/TUFFC.2024.3409518

Highlights

- **A forked microvascular phantom has been designed to test the performance of ultrasound localization microscopy (ULM) in a bifurcation scenario with uniformly increasing flow channel separation.**
- **The forked lumen core's measured mean width (252±15 μm) and flow channel separation gradient (50.89 μm/mm) corresponded well with the design dimensions.**
- **As an *in vitro* test platform for ULM performance investigations, the new phantom will help refine the maturity of ULM solutions for the visualization of microvessels.**

In designing a ULM algorithm, one experimental question that needs to be addressed is how to methodically characterize the algorithm's microvascular resolving power. Present in vivo testing methodology typically involves a comparison between the ULM-resolved vascular features and the corresponding optical microscopy images at the same site [16]. Yet, such a comparative analysis is challenging to perform when examining vascular features that are deeper than the penetration limit of optical microscopy. Some studies have performed post-hoc comparisons of the effects of novel algorithm implementations [3] and testing methodology [13] on localization outcomes, but they are inherently unable to determine a ULM technique's resolving power due to the lack of ground truth knowledge on the microvascular anatomy. Alternatively, long-duration acquisition studies show promise in generating a cross reference for accuracy assessment. Nonetheless, for this approach, practical hurdles are present in vivo because, over the duration (up to 40 min) required to form a reference image comparable to the resolution of optical microscopy (~5 μm), motion artifacts are prone to arise even for well-controlled anesthetic conditions [13].

Considering the challenges behind native in vivo studies, it is appropriate to perform in vitro phantom validation of ULM algorithms prior to in vivo experimentation [6], [17]. However, there is currently a lack of a compelling in vitro test protocol that is dedicated to ULM performance evaluation. Some studies used single-tube models for performance calibration, but they inherently do not allow for the assessment of channel resolvability in normal [18], [19] or modified imaging environments [20]. Although a few crossed micro-tube configurations have been reported [21], [22], [23], they after all involved separate flow channels and lacked resemblance of microvascular branching characteristics. Attempts using lithography to produce straight [24] or bifurcating ULM phantoms [25] have also been made, but they are limited in their representation of soft tissue because their build material typically has acoustic properties (acoustic speed, attenuation) that are different from those for soft tissue [26], [27]. Efforts to devise 3-D-printed ULM phantoms with ultrasound-compatible materials also suffer from mediocre print stability and positioning errors [28]. A suitable ULM phantom with matched acoustic properties and vascular branching features has yet to be developed.

Here, we present the design and development of a new framework for creating an acoustically compatible microvascular phantom with uniformly increasing flow channel separation that serves well as a calibration feature for ULM performance testing. Our design is guided by two propositions: 1) bifurcating flow features commonly found in capillaries can be approximated as a forked lumen geometry that is cast within a tissue mimicking slab and 2) the rate of channel separation in the forked lumen geometry can be precisely controlled by defining the bifurcation angle of the forked lumen, as can be realized using computer aided design (CAD) tools. Accordingly, we have devised a microvascular phantom design protocol that involves CAD design, additive manufacturing, and lost-core casting to develop an in vitro testing platform that is representative of microvascular flow. As will be shown in this article, when connected to a microflow circuit, our phantom's forked lumen can effectively mimic microvascular flow characteristics that are useful for ULM performance analysis.

II. Phantom Design Protocol

A. Design of the Forked Microvascular Lumen Core

As shown in Fig. 1(a), our phantom's forked lumen comprised two sub-segments: 1) a straight-tube common inlet (15 mm length) and 2) a V-shaped flow channel pair (20 mm length span). This lumen geometry can be considered as an analog to a microvascular bifurcation segment with common and discrete channel regions. From trigonometry principles, it is well known that the post-bifurcation separation gradient is linear for this V-shaped flow channel pair. This design feature is important to the testing of an ULM method's resolving power in distinguishing two adjacent flow channels with similar flow dynamics but with linearly varying separation distance.

The forked lumen core was drafted in SolidWorks (Dassault, Systemes, Waltham, MA, USA). As shown in Fig. 1(b), the outlets of the V-shaped flow channel pair are axially spaced at 1 mm apart (measured edge to edge). For this pair of bifurcating flow channels, the corresponding flow channel separation increased at a rate of 50 μm/mm. The corresponding bifurcation angle was 2.9°. The flow channel diameter was set to 250 μm, which corresponds to the smallest size that could be consistently fabricated with a powder-bed fusion system. Note that, as explained in Section V-B, although this flow channel diameter is larger than typical capillary sizes, it is not a critical consideration in the context of using the forked lumen for ULM resolving power analysis.

To facilitate the fabrication of a physical replicate of the forked lumen core via additive manufacturing, this geometry

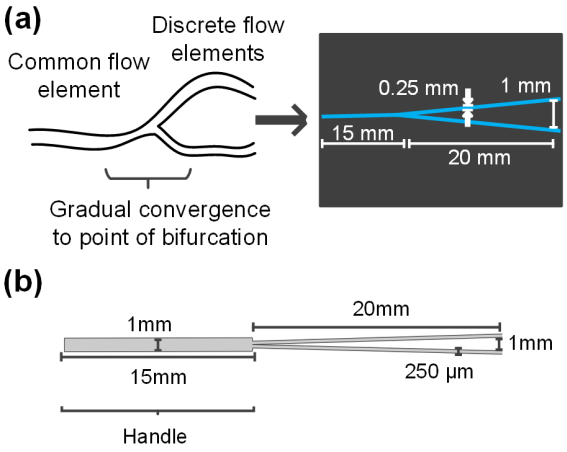

Fig. 1. Forked microvascular lumen core. (a) The bifurcating feature of a microvessel segment is mimicked using a Y-shaped channel design with an initial edge-to-edge spacing of 1 mm converging into a single channel 20 mm into the phantom. (b) CAD draft of the forked lumen core that is used to create flow channels (250 μm width, 2 mm height) within a tissue mimic cast.

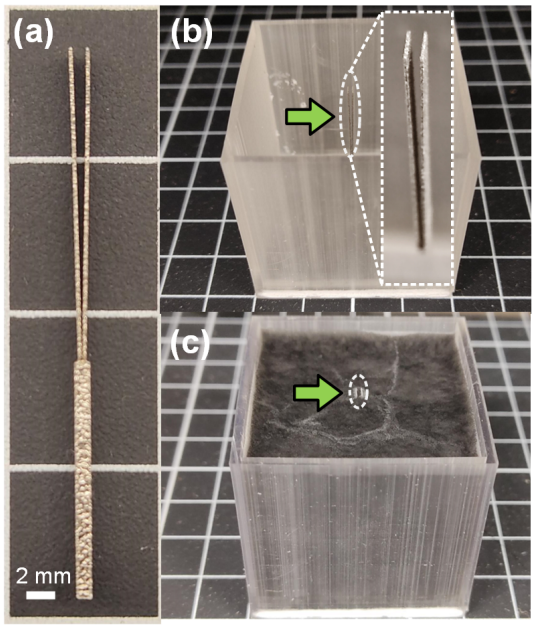

Fig. 2. Phantom fabrication process. (a) Image of the microvascular lumen core's physical replicate. (b) The Lumen core (circled gray) was positioned in a vertical orientation within a sacrificial container using hot melt adhesive prior to casting PVA tissue mimic in the box (Inset: microscope image of the core overlooking both channels). (c) Sacrificial container partially filled with PVA to the intended level.

was extended in the azimuthal direction by 2 mm in SolidWorks. As shown in Fig. 1(b), to enable subsequent connection of the forked lumen to the flow circuit, the core's common flow inlet segment was expanded to a 1 mm-width rectangular handle.

B. Fabrication Procedure

The drafted lumen core was exported and transferred to an external facility (Multi-Scale Additive Manufacturing Laboratory, Kitchener, ON, Canada) for fabrication. Physical replicas, a photograph of which is shown in Fig. 2(a), were created via powder-bed fusion additive manufacturing system (AM400; Renishaw, Wotton-under-Edge, Gloucestershire, U.K.), with 80 W power, 70 μs exposure time, and 90 μm point distance. Inconel 625 powder (15–45 μm particle size; Renishaw) was used as the additive manufacturing material since it was known for its high strength properties as a nickel-chromium alloy.

Modifying from our earlier protocol [29], we coated the forked lumen core in petrolatum and mounted it in an upright orientation within a sacrificial casting container using hot melt adhesive shown in Fig. 2(b) to facilitate tissue mimic casting. The casting container, also drafted using SolidWorks and fabricated with a resin 3-D printer (Saturn; Elegoo, Shenzhen, China), had interior dimensions of 40 × 40 × 40 mm (length × width × height). A polyvinyl alcohol (PVA)-based tissue mimicking mixture was then poured into the casting container, as shown in Fig. 2(c), until the mixture height was slightly below the prongs of the branched region. The PVA formula comprised 88.7% (wt%) degassed water, 10% PVA (341584; Sigma-Aldrich, St. Louis, MO, USA), 1% graphite as acoustic scatterers (282863; Sigma-Aldrich), and 0.3% potassium sorbate (85520; Sigma-Aldrich) [29]. Prior to casting, the PVA mixture was magnetically stirred at 90 °C for 1 h and was allowed to degas overnight at room temperature.

The PVA-loaded container with the forked lumen core was subjected to a 24 h freeze cycle at −20 °C followed by a 24-h thaw cycle at 4 °C to allow the slab to congeal. This freeze and-thaw cycle was repeated three times. The corresponding speed of sound and attenuation coefficient of the congealed PVA slab are respectively 1535 m/s and 0.229 dB/(cm·MHz) as previously reported [29].

After the freeze-and-thaw cycles, the walls of the container were removed, while the base of the container was extracted with the phantom. Subsequently, the V-shaped flow channel pair was formed by withdrawing the cast core from the PVA slab. To prevent residual PVA from accumulating on the extracted core, the core removal step was realized by gently pulling on the handle of the cast core with pliers.

C. Flow Circuitry and Introduction of Contrast

The flow channel of the PVA slab was oriented in an upright configuration as shown in Fig. 3. Its common flow inlet at the bottom was connected to a 20 mL syringe via silicone tubing (1 mm inner diameter; 2 mm outer diameter). The flow channel was first washed with degassed water. After that, Definity-like MBs, fabricated using an in-house sonication protocol [30], were added to the syringe in a diluted form with degassed water in different concentrations ranging from 1.5×10^5 to 10^7 bubbles/mL. The syringe was stirred to mix the solution. Flow was then introduced at different flow rates ranging from 1.67 to 167 μL/s. The contents were perfused for 30 s prior to imaging experiments.

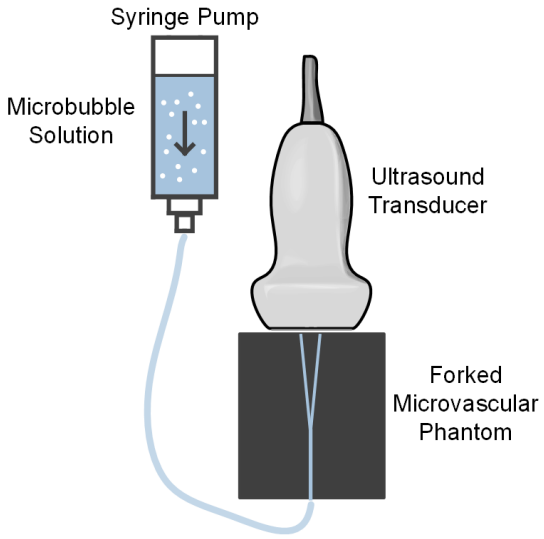

Fig. 3. Illustration of the flow circuit used to infuse MBs through the forked microvascular phantom. Flow was fed at rates ranging from 1.67 to 167 μL/s through a connection to the common channel of the phantom. The transducer was positioned directly at the top surface of the phantom above the feature to cut across both channels.

III. Experimental Methods

A. Measurement of Phantom Core Replicate Geometry

Prior to PVA casting, the forked lumen core that was fabricated using additive manufacturing was imaged using an optical microscope (Celestron Handheld Digital Microscope; Celestron, Torrance, CA, USA) to obtain reference values for flow channel dimensions. These optical images were obtained under 55× magnification with a reference scale attached. The acquired images were imported into ImageJ (U.S. National Institutes of Health, Bethesda, MD, USA) to obtain measurements of flow channel width and separation. After the casting process, each extracted core was reexamined under microscopy to check their shape.

B. ULM Data Acquisition Setup

Ultrasound contrast imaging data was collected using unsteered plane wave transmissions from a SonixTouch ultrasound scanner (Analogic Ultrasound, Peabody, MA, USA) with a 128-element linear array (L14-5; Analogic Ultrasound) that was attached to a mechanical micropositioner. The transducer was aligned to the image across both channels in the flow parallel axis. Imaging was conducted with three-cycle, 5 MHz ultrasound pulses, a pulse repetition frequency of 1000 Hz, and an acquisition period up to 20 s. Raw radio frequency (RF) channel data was acquired using a SonixDAQ attachment (Analogic Ultrasound) with a sample rate of 40 MHz [31].

C. Localization Processing Framework

RF channel data were transferred and processed on a GPU workstation using MATLAB (2016a, Mathworks, Natick, MA, USA). A 30th-order finite-impulse-response (FIR) bandpass filter (3–7 MHz passband) was applied to the channel data to suppress out-of-band white noise before beamforming. Data were processed to generate images using a delay-and-sum beamformer as previously presented [32]. A single B-mode image was beamformed with dimensions of 38 × 30 mm^2 (lateral × axial). An area of interest containing contrast signals denoted by high signal intensity was manually identified. All 20 000 frames were then beamformed using a smaller 4 × 12 mm^2 (400 × 600 pixels, 10 μm lateral pixel size, 20 μm axial pixel size) window at the area of interest to reduce processing time. A 134th-order FIR highpass filter (cutoff at 50 Hz) was applied on the slow-time axis to remove stationary tissue clutter. Localization imaging was achieved through the application of a bubble detection and deconvolution-based framework similar to what was previously reported [2]. The filtered image was cross-correlated with the scanner's point spread function to detect MB positions, and output threshold was set to 50% of the maximum cross correlation value to suppress noncontrast signal. To pinpoint the spatial location of the bubble signal, the cross correlated images were deconvolved using the Richardson-Lucy deconvolution method [33], [34]. The mean of the 20 000-frame stack was taken to form ULM images.

D. Lumen Width and Flow Channel Separation Measurements

Lumen center and width were determined by Gaussian fitting to the cross-sectional profile of the resolved lumens and extracting the full-width-at-half-maximum (FWHM) of the fits. The separation distance between the two post-bifurcation flow channels (edge-to-edge) was obtained by subtracting half of the widths of both lumens from the center-to-center distance. Five measurements were taken for ULM images formed from 10 s of acquisition with a 2 s sliding window between each set.

IV. Results

A. Optical Imaging Confirms Dimensions of the Fabricated Forked Lumen Core

The forked lumen core fabricated using additive manufacturing was found to have dimensions that are close to the design dimensions. Fig. 4(a) shows the lumen core's channel width, post-bifurcation flow channel separation, and separation gradient measurements observed under an optical microscope. The cross-sectional width of the lumen core was measured at points perpendicular to the axis of symmetry with examples shown in green markers of the left inset in Fig. 4(a). The mean width of the core measured under optical microscopy was 252 ± 15 μm (mean ± s.d.), which corresponds to a mean error of 0.8% with respect to the design diameter of 250 μm.

Optical microscopy measurements for the edge-to-edge separation at a given distance away from the bifurcation point are illustrated as blue markers of the right inset of Fig. 4(a). The measured separation points are depicted in Fig. 4(b) together with the regression line (black) for the separation gradient taken from optical measurements and the theoretical

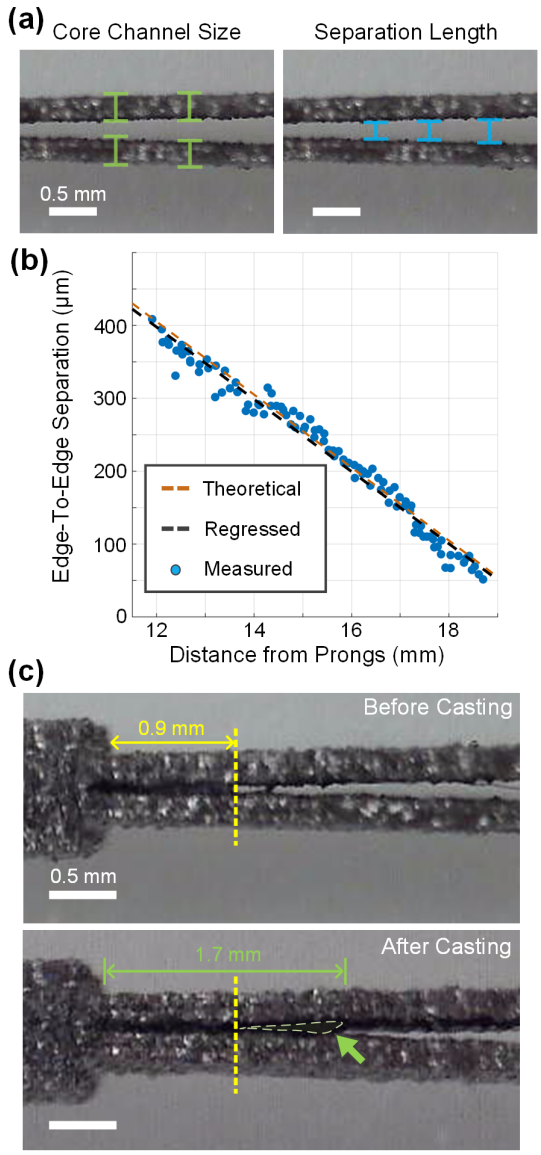

Fig. 4. Optical images and size measurements of the fabricated forked lumen core. (a) Using ImageJ, the channel width (green) and channel-to-channel separation distance (blue) were measured at different sections of the lumen core. (b) The plot of the measured inner edge separation (blue dots), corresponding regression line (black-dashed), and theoretical separation gradient (orange-dashed). (c) Image comparison between a precast core that was brushed with petrolatum (unremovable excess at yellow line) to reduce surface roughness and a post-cast core containing PVA pullout (indicated by the green arrow).

(orange) separation gradient derived from the CAD drawing. The measured channel separation gradient was found to be 50.9 μm/mm, which is 1.8% different from the theoretical separation rate of 50 μm/mm.

As shown in Fig. 4(c), the fabricated lumen core was found to remain intact in shape during the casting process. Nonetheless, in the separation space between the two diverging channels, there was some excess petrolatum coating and residual PVA near the bifurcation point, as indicated by the yellow dashed line and the green arrow in Fig. 4(c). The axial length of this excess zone was measured to be 1.7 mm (of which 0.9 mm was attributed to the excess petrolatum coating).

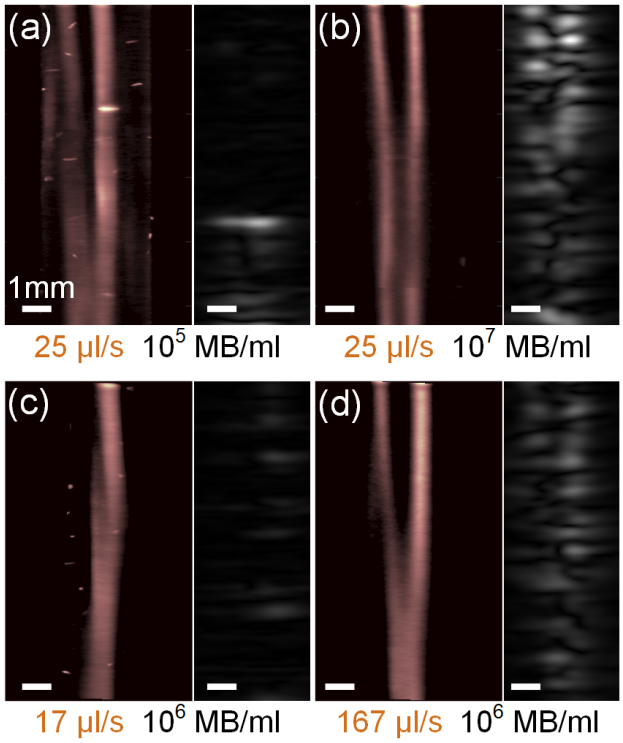

Fig. 5. ULM images of the new phantom's microflow channels for the following flow rates and MB concentrations (a) 25.3 μL/s, 1.5×10^5 MB/mL; (b) 25.3 μL/s, 1.5×10^7 MB/mL; (c) 16.7 μL/s, 1.5×10^6 MB/mL; and (d) 167 μL/s, 1.5×10^6 MB/mL. Note that in (c), the left-side channel is missing because of insufficient flow to that area. Corresponding B-mode image frames are also shown as reference.

As such, the new phantom's V-shaped flow channel pair had effectively merged at an axial distance of 18.3 mm away from the two flow outlets.

B. Flow Channels in the Forked Microvascular Phantom Can Be Consistently Visualized Using ULM

When ULM is performed on the new phantom, the V-shaped flow channel pair can generally be detected if appropriate ULM parameters are used. Fig. 5 shows a set of ULM images for a 20 s acquisition period, different flow rates (16.7, 25.3, and 167 μL/s), and MB concentrations (1.5×10^5, 1.5×10^6, and 1.5×10^7 MB/mL). For reference, a corresponding B-mode image for each parameter combination is shown in parallel. Three observations can be noted from this figure. First, as shown in Fig. 5(d), for a 20-s acquisition period, the V-shaped channel is better visualized with a flow rate of 167 μL/s and an MB concentration of 1.5×10^6 MB/mL. Second, as illustrated in Fig. 5(a) and (b), at a slower flow rate of 25.3 μL/s, the use of a higher MB concentration (1.5×10^7 instead of 1.5×10^5 MB/mL) has improved the resulting visualization of the V-shaped channel. Third, as shown in Fig. 5(c), when the flow rate was further lowered to 16.7 μL/s, the V-shaped channel cannot be consistently visualized because of insufficient flow to one of the branches. In all these cases, the V-shaped flow channel pair is not visible in the corresponding B-mode images.

C. ULM Visualization of the Forked Microvascular Phantom at Different Acquisition Times

As a further investigation of ULM's microvascular imaging performance, Fig. 6 shows a series of ULM images (left inset of each subfigure) at four acquisition times of the same experiment run (from 2 to 8 s). It can be observed that visualization of the phantom's bifurcating lumen gradually improved as the acquisition time is progressively lengthened from 2 to 8 s. Also shown in Fig. 6 are the corresponding cross section profiles at two locations downstream from the bifurcation point (the two right insets of each subfigure). Channel widths and centers, as determined via Gaussian fitting, are depicted in the cross section profiles where the orange and blue overlays in Fig. 6(a)–(d) are, respectively, the left (orange) and right (blue) lumen regions of the corresponding cross sections. As can be observed, these cross section profiles progressively become less noisy for longer acquisition times. It is also interesting to note that, at all four acquisition times, both branches of the forked phantom have been depicted in the cross section profiles, even though the left and right flow channels have different intensity levels due to image plane misalignment during ULM data acquisition.

Quantitative analysis of ULM-measured flow channel widths revealed that ULM's resolving power became stabilized when the acquisition time approached 10 s. Corresponding data are provided in Fig. 7(a) which shows the Gaussian-fit FWHM of the right channel (mean $\pm$ s.d.; $N = 5$) at different imaging depths (from 12 to 16.5 mm; in 0.5 mm increments) as a function of acquisition time (from 0 to 10 s; 0.25 s intervals). As can be noted, at greater axial depths that are closer to the bifurcation point (e.g., 16 and 16.5 mm), the estimated flow channel width exhibited high standard deviation when the acquisition time was only a few seconds. Such an estimation variance was progressively reduced as acquisition time was lengthened. In contrast, at shallower depths where the flow channels are more separated, the variance of the estimated flow channel width remained low even at short acquisition times.

D. Flow Channel Width and Separation Distance Derived From ULM Measurements

Another noteworthy trend of Fig. 7(a) is that ULM-measured flow channel widths are larger than the optically measured mean width of 252 μm (as mentioned in Section IV-A). Specifically, at 12 mm depth where the two flow channels are in theory separated by 400 μm, the estimated flow channel width was 320 μm. At depths near the forked phantom's bifurcation point, the estimated flow channel width was found to be even larger and, correspondingly, ULM's resolving power was lower for these imaging depths. In particular, at 16.5 mm depth, the Gaussian-fit FWHM of the right flow channel was 630 μm.

To further characterize ULM's resolving power, Fig. 7(b) plots, as a function of imaging depth, the relative ULM-measured flow channel width with respect to the mean width of 252 μm measured using optical microscopy as presented in Section IV-A. In general, ULM was found to yield flow channel width measurements that were larger than the optically measured width of the forked lumen core. Also, an increase trend in the relative ULM-measured flow channel width can be observed as the imaging depth increases

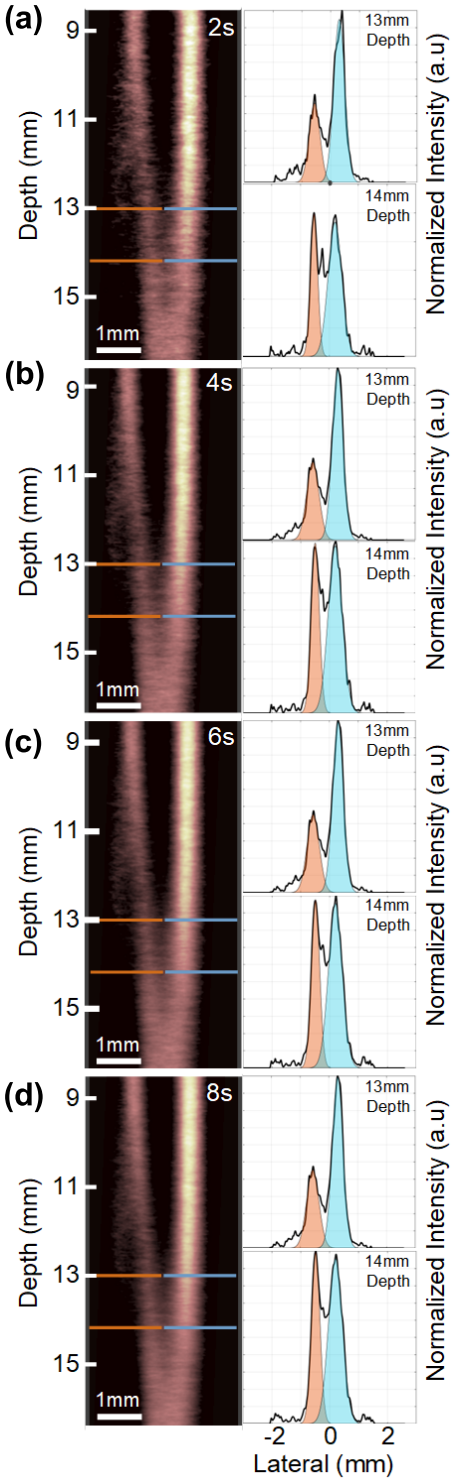

Fig. 6. Cross section analysis of ULM images of the forked microvascular phantom at increasing acquisition times of (a) 2 s, (b) 4 s, (c) 6 s, and (d) 8 s at depths of 13 and 14 mm. FWHM of each channel was determined by Gaussian fits illustrated in orange and blue for left and right channels respectively. Bubbles were infused at 167 μL/s with concentration of 1.5×10^6 MB/mL.

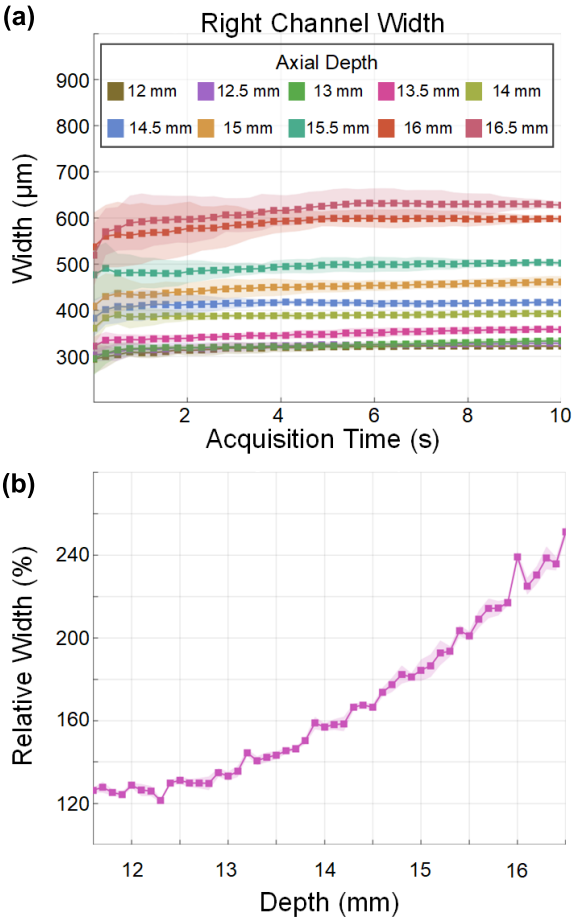

Fig. 7. ULM-measured width of the right flow channel in the forked microvascular phantom. (a) Average Gaussian-fit FWHM ($N = 5$) measured at different axial depths from the flow outlet as a function of acquisition time (the shaded zone of each line depicts standard deviation). (b) Relative flow channel width (with reference to the optically measured mean width of 252 μm) at different axial depths from the flow outlet.

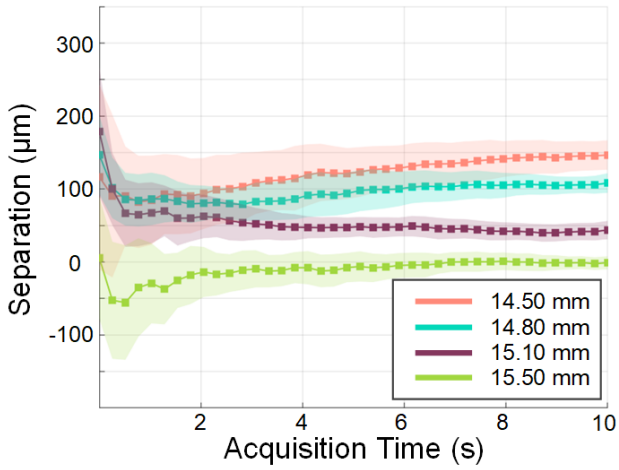

Fig. 8. ULM-measured channel-to-channel separation distance in the forked microvascular phantom as a function of acquisition time for four axial depths: 14.5 mm (orange), 14.8 mm (blue), 15.10 mm (purple), and 15.50 mm (green).

(i.e., as we approach the forked phantom's bifurcation point). At 12 mm depth, the relative ULM-measured flow channel width was 127% of the optically measured width; in contrast, at 16.5 mm, this relative width was increased to 240%.

As a more detailed analysis, Fig. 8 plots the ULM-measured flow channel separation distance of the two post-bifurcation flow channels as a function of data acquisition time from 0 to 10 s (with 0.25 s intervals). Results are shown for four imaging depths: 14.5 mm (orange), 14.8 mm (cyan), 15.1 mm (purple), and 15.5 mm (green). As can be observed, at these four depths, the corresponding edge-to-edge separation distance of the two flow channels converged to 150, 110, 50, and 0 μm (at 10 s acquisition period). These separation distance measurements converged when the acquisition time was 8 s or longer.

V. Discussion

A. Summary of Methodological Contributions

As a new microvascular mapping technique, ULM has garnered significant attention in recent years. To facilitate this technique's performance analysis, simulation-based approaches have been adopted to synthesize ULM data for different vascular geometries [35], [36]. Nevertheless, these in silico solutions inherently cannot be used to evaluate the experimental performance of ULM setups that are subjected to hardware noise and that use real contrast agents. In contrast, this article has presented a new forked microvascular phantom that can be used for in vitro assessment of an ULM method's resolving power. Its lumen was designed as a bifurcation geometry with a linear flow channel separation gradient downstream from the bifurcation (see Fig. 1). It was fabricated using additive manufacturing and was used to form a wall-less forked microvascular phantom via lost-core casting principles (see Fig. 2). The dimensions of the fabricated forked lumen core were closely aligned with the design dimensions (see Fig. 4).

The key technical merit of our new phantom is that it is the first ULM performance calibration phantom with: 1) a pair of flow channels that have a uniformly increasing separation and that lie on the same plane and 2) an ultrasound-compatible tissue mimicking slab that encompasses the microvascular lumen. The first feature is critical in determining what is the minimum flow channel separation distance that can be detected by ULM. It is seemingly more expedient to use our new phantom for such an analysis as opposed to devising multiple phantoms involving parallel flow channel pairs with different separation distances. The second feature is important too as it can effectively avoid aberration (due to speed of sound mismatch) that may hamper contrast echo localization performance and provide background noise to simulate live tissue.

B. Application of New Phantom in ULM Experiments

When our new phantom was used to perform ULM experiments (see Fig. 3), it was found to be useful in characterizing the resolving power of a previously reported ULM algorithm (see Fig. 5). It also facilitated systematic analysis of the impact of acquisition time on ULM image quality and its resolvability of adjacent flow channels. In general, results

have confirmed that longer acquisition times are important to generate high-quality ULM images of the forked lumen geometry (see Fig. 6). Note that the intensity of the left and right flow channels may not be identical depending on the image plane placement during ULM data acquisition. This issue is after all inevitable because the phantom's forked lumen is after all just 250 μm in size and thus it is not possible to use B-mode imaging for navigation and precise alignment of the image plane to the forked lumen. Nevertheless, the two flow channels can be distinguishably visualized and did not affect our phantom's ability to facilitate testing of ULM's microvascular resolving power.

In our ULM characterization analyses, overestimation was found in the measured flow channel widths (see Fig. 7). This issue was more significant at greater axial depths near the lumen's bifurcation point because the narrow channel-to-channel separation distance has made it challenging for the ULM algorithm to properly discern between the two flow channels. Correspondingly, the ULM-measured channel-to-channel separation distance was underestimated and became zero at an axial depth of 15.5 mm (see Fig. 8) that supposedly had a separation distance of 229 μm [for a measured separation gradient of 50.9 μm/mm as per Fig. 4(b)]. These findings generally prompt the need to enhance ULM's resolving power through the design of more advanced algorithms.

C. Choice of Material for Phantom Fabrication

The focus of this work has been to establish the methodology of preparing a forked microvascular phantom. In this process, we have used an established PVA mixture formula [29] to form our tissue-mimicking material. One potential concern of such a phantom fabrication approach is that the corresponding freeze-thaw process, which naturally leads to mild physical contraction and expansion of the hydrogel slab to foster PVA crosslinking, might unintentionally deform the forked lumen core. To circumvent this issue, we have devised a lumen core fabrication protocol that is based on additive manufacturing using a metallic, mechanically tough nickel-chromium alloy material (Inconel 625 powder). Accordingly, the lumen of our developed phantom has largely maintained its V-shaped geometry. Note that, in our preliminary work, we initially attempted to build the forked lumen core via 3-D printing of polylactic acid (PLA) filaments. We found that, when these 3-D printed lumen cores were used for lost-core casting, the resulting V-shaped flow channel pair was slightly bent near the two flow outlets due to the lighter weight and lower rigidity of the PLA material (data not shown).

Our PVA mixture formula was based on the use of graphite as acoustic scatterers [29], so the phantom's corresponding tissue-mimicking slab was optically dark. In the future, it is worth investigating the use of other formulations for tissue-mimicking materials [37]. One direction worth pursuing is the development of a transparent tissue-mimicking material, since the current use of graphite in our formula has naturally made the tissue slab opaque and, in turn, has inhibited any optical validation of the flow channels. Alternatively, it may be helpful to perform microcomputed tomography [38] scans to obtain the necessary ground truth needed to validate our phantom's fidelity in resembling the forked lumen that we have drafted using CAD. Another related topic that is worth examining further is how different acoustic scatterer concentrations would affect the background tissue signal and, in turn, influence the microvascular resolving power of a ULM algorithm. This study can be performed by developing a library of forked microvascular phantoms with different tissue-mimicking material compositions and using them to test ULM algorithms.

D. Limitations of Phantom Fabrication Protocol

It should be noted that the minimum flow channel diameter that can be supported in our phantom design protocol is currently constrained by the print resolution of our additive manufacturing system. In this work, we have demonstrated that it is possible to fabricate forked lumen cores with widths near the design dimension of 250 μm and a designed separation rate of 50 μm/mm. Although this flow channel diameter is larger than typical capillary diameters (which can be down to a few microns), it is fortunately not a critical drawback because ULM's resolving power can be analyzed by leveraging the phantom's V-shaped flow channel pair (with uniformly increasing post-bifurcation separation). Yet, as a future endeavor, it would still be beneficial to devise forked lumen cores with smaller diameters through the use of more advanced systems that have fingerprint resolution than the one used in this investigation.

Another nonideality of our phantom design protocol is that, during the lumen core pullout step that served to form the V-shaped flow channel pair, some congealed PVA remained attached to the crevice at the branching point [see Fig. 4(c)]. This issue is unavoidable due to the acute angle at the branch point of the forked lumen core. Nevertheless, the extent of this problem is limited because the attachment zone has only axially spanned 1.7 mm from the bifurcation point. The corresponding V-shaped flow channel pair has still spanned an axial length of 18.3 mm between the two flow outlets and the effective merge point (i.e., 1.7 mm axial distance away from the theoretical bifurcation point). Accordingly, the minimum channel-to-channel separation of our phantom (i.e., adjacent to the effective merge point) was deduced to be equal to 86.5 μm based on the channel separation gradient shown in Fig. 4(b).

VI. Conclusion

In recent years, ULM and super-resolution ultrasound imaging solutions have been actively developed for microvascular visualization applications. However, these algorithmic innovation endeavors have yet to be matched with representative in vitro models for performance calibration and testing prior to in vivo application. Here, we have devised a forked microvascular phantom that was modeled after a bifurcation point. With known design dimensions and its V-shaped flow channel pair feature, our new phantom can be used to quantitatively analyze the microvascular resolving power of ULM methods. Overall, this in vitro test platform will help translate new ULM techniques toward practical use to improve clinical visualization of microvascular pathologies.

REFERENCES

[1] E. Betzig et al., "Imaging intracellular fluorescent proteins at nanometer resolution," *Science*, vol. 313, no. 5793, pp. 1642–1645, Sep. 2006.

[2] S. Lei et al., "In vivo ultrasound localization microscopy imaging of the Kidney's microvasculature with block-matching 3-D denoising," *IEEE Trans. Ultrason., Ferroelectr., Freq. Control*, vol. 69, no. 2, pp. 523–533, Feb. 2022.

[3] J. R. McCall et al., "Longitudinal 3-D visualization of microvascular disruption and perfusion changes in mice during the evolution of glioblastoma using super-resolution ultrasound," *IEEE Trans. Ultrason., Ferroelectr., Freq. Control*, vol. 70, no. 11, pp. 1401–1416, Nov. 2023.

[4] T. Opacic et al., "Motion model ultrasound localization microscopy for preclinical and clinical multiparametric tumor characterization," *Nature Commun.*, vol. 9, no. 1, p. 1527, 2018.

[5] B. Huang et al., "Acceleration-based Kalman tracking for super-resolution ultrasound imaging in vivo," *IEEE Trans. Ultrason., Ferroelectr., Freq. Control*, vol. 70, no. 12, pp. 1739–1748, Dec. 2023.

[6] F. Lin, S. E. Shelton, D. Espindola, J. D. Rojas, G. F. Pinton, and P. A. Dayton, "3-D ultrasound localization microscopy for identifying microvascular morphology features of tumor angiogenesis at a resolution beyond the diffraction limit of conventional ultrasound," *Theranostics*, vol. 7, pp. 196–204, Jan. 2017.

[7] J. Yu, L. Lavery, and K. Kim, "Super-resolution ultrasound imaging method for microvasculature in vivo with a high temporal accuracy," *Sci. Rep.*, vol. 8, no. 1, p. 13918, Sep. 2018.

[8] D. Fukumura and R. K. Jain, "Tumor microvasculature and microenvironment: Targets for anti-angiogenesis and normalization," *Microvascular Res.*, vol. 74, pp. 72–84, Sep./Nov. 2007.

[9] M. J. Mulligan-Kehoue, "The vasa vasorum in diseased and nondiseased arteries," *Amer. J. Physiol.-Heart Circulatory Physiol.*, vol. 298, pp. H295–H305, Nov. 2009.

[10] J. Attems and K. A. Jellinger, "The overlap between vascular disease and Alzheimer's disease–lessons from pathology," *BMC Med.*, vol. 12, p. 206, Nov. 2014.

[11] S. Harput et al., "Two-stage motion correction for super-resolution ultrasound imaging in human lower limb," *IEEE Trans. Ultrason., Ferroelectr., Freq. Control*, vol. 65, no. 5, pp. 803–814, May 2018.

[12] K. Christensen-Jeffries et al., "Poisson statistical model of ultrasound super-resolution imaging acquisition time," *IEEE Trans. Ultrason., Ferroelectr., Freq. Control*, vol. 66, no. 7, pp. 1246–1254, Jul. 2019.

[13] V. Hingot, C. Errico, B. Heiles, L. Rahal, M. Tanter, and O. Couture, "Microvascular flow dictates the compromise between spatial resolution and acquisition time in ultrasound localization microscopy," *Sci. Rep.*, vol. 9, no. 1, p. 2456, Feb. 2019.

[14] D. Ghosh, F. Xiong, S. R. Sirsi, P. W. Shaul, R. F. Mattrey, and K. Hoyt, "Toward optimization of in vivo super-resolution ultrasound imaging using size-selected microbubble contrast agents," *Med. Phys.*, vol. 44, no. 12, pp. 6304–6313, Oct. 2017.

[15] F. Lin, J. K. Tsuruta, J. D. Rojas, and P. A. Dayton, "Optimizing sensitivity of ultrasound contrast-enhanced super-resolution imaging by tailoring size distribution of microbubble contrast agent," *Ultrasound Med. Biol.*, vol. 43, no. 10, pp. 2488–2493, Oct. 2017.

[16] K. Christensen-Jeffries et al., "Super-resolution ultrasound imaging," *Ultrasound Med. Biol.*, vol. 46, no. 4, pp. 865–891, 2020.

[17] E. Kanoulas et al., "Super-resolution contrast-enhanced ultrasound methodology for the identification of in vivo vascular dynamics in 2D," *Investigative Radiol.*, vol. 54, pp. 500–516, Aug. 2019.

[18] O. M. Viessmann, R. J. Eckersley, K. Christensen-Jeffries, M. X. Tang, and C. Dunsby, "Acoustic super-resolution with ultrasound and microbubbles," *Phys. Med. Biol.*, vol. 58, no. 18, pp. 6447–6458, Sep. 2013.

[19] W. Gu, B. Li, J. Luo, Z. Yan, D. Ta, and X. Liu, "Ultrafast ultrasound localization microscopy by conditional generative adversarial network," *IEEE Trans. Ultrason., Ferroelectr., Freq. Control*, vol. 70, no. 1, pp. 25–40, Jan. 2023.

[20] M. A. O'Reilly and K. Hynynen, "A super-resolution ultrasound method for brain vascular mapping," *Med. Phys.*, vol. 40, no. 11, Nov. 2013, Art. no. 110701.

[21] G. Zhang et al., "Acoustic wave sparsely activated localization microscopy (AWSALM): Super-resolution ultrasound imaging using acoustic activation and deactivation of nanodroplets," *Appl. Phys. Lett.*, vol. 113, no. 1, Jul. 2018, Art. no. 014101.

[22] S. Harput et al., "3-D super-resolution ultrasound imaging with a 2-D sparse array," *IEEE Trans. Ultrason., Ferroelectr., Freq. Control*, vol. 67, no. 2, pp. 269–277, Feb. 2020.

[23] Z. Dong et al., "High volume rate 3-D ultrasound imaging using fast-tilting and redirecting reflectors," *IEEE Trans. Ultrason., Ferroelectr., Freq. Control*, vol. 70, no. 8, pp. 799–809, Aug. 2023.

[24] Y. Desailly, J. Pierre, O. Couture, and M. Tanter, "Resolution limits of ultrafast ultrasound localization microscopy," *Phys. Med. Biol.*, vol. 60, no. 22, pp. 8723–8740, Nov. 2015.

[25] Y. Desailly, O. Couture, M. Fink, and M. Tanter, "Sono-activated ultrasound localization microscopy," *Appl. Phys. Lett.*, vol. 103, no. 17, Oct. 2013, Art. no. 174107.

[26] S. S. M. Lai, B. Y. S. Yiu, A. K. K. Poon, and A. C. H. Yu, "Design of anthropomorphic flow phantoms based on rapid prototyping of compliant vessel geometries," *Ultrasound Med. Biol.*, vol. 39, no. 9, pp. 1654–1664, Sep. 2013.

[27] A. C. O. Tsang et al., "Blood flow in intracranial aneurysms treated with Pipeline embolization devices: Computational simulation and verification with Doppler ultrasonography on phantom models," *Ultrasonography*, vol. 34, no. 2, pp. 98–108, Jan. 2015.

[28] M. L. Ommen, M. Schou, C. Beers, J. A. Jensen, N. B. Larsen, and E. V. Thomsen, "3D printed calibration micro-phantoms for super-resolution ultrasound imaging validation," *Ultrasonics*, vol. 114, Jul. 2021, Art. no. 106353.

[29] C. K. Ho, A. J. Y. Chee, B. Y. S. Yiu, A. C. O. Tsang, K. W. Chow, and A. C. H. Yu, "Wall-less flow phantoms with tortuous vascular geometries: Design principles and a patient-specific model fabrication example," *IEEE Trans. Ultrason., Ferroelectr., Freq. Control*, vol. 64, no. 1, pp. 25–38, Jan. 2017.

[30] C. A. Schneider, W. S. Rasband, and K. W. Eliceiri, "NIH image to ImageJ: 25 years of image analysis," *Nature Methods*, vol. 9, no. 7, pp. 671–675, Jun. 2012.

[31] C. C. P. Cheung et al., "Multi-channel pre-beamformed data acquisition system for research on advanced ultrasound imaging methods," *IEEE Trans. Ultrason., Ferroelectr., Freq. Control*, vol. 59, no. 2, pp. 243–253, Feb. 2012.

[32] B. Y. S. Yiu, I. K. H. Tsang, and A. C. H. Yu, "GPU-based beamformer: Fast realization of plane wave compounding and synthetic aperture imaging," *IEEE Trans. Ultrason., Ferroelectr., Freq. Control*, vol. 58, no. 8, pp. 1698–1705, Aug. 2011.

[33] W. H. Richardson, "Bayesian-based iterative method of image restoration," *J. Opt. Soc. Amer.*, vol. 62, no. 1, pp. 55–59, Jan. 1972.

[34] L. B. Lucy, "An iterative technique for the rectification of observed distributions," *Astronomical J.*, vol. 79, pp. 745–754, Jun. 1974.

[35] J. R. McCall, P. A. Dayton, and G. F. Pinton, "Characterization of the ultrasound localization microscopy resolution limit in the presence of image degradation," *IEEE Trans. Ultrason., Ferroelectr., Freq. Control*, vol. 69, no. 1, pp. 124–134, Jan. 2022.

[36] X. Chen, M. R. Lowerison, Z. Dong, A. Han, and P. Song, "Deep learning-based microbubble localization for ultrasound localization microscopy," *IEEE Trans. Ultrason., Ferroelectr., Freq. Control*, vol. 69, no. 4, pp. 1312–1325, Apr. 2022.

[37] C. K. McGarry et al., "Tissue mimicking materials for imaging and therapy phantoms: A review," *Phys. Med. Biol.*, vol. 65, Sep. 2020, Art. no. 23TR01.

[38] C. Huang et al., "Short acquisition time super-resolution ultrasound microvessel imaging via microbubble separation," *Sci. Rep.*, vol. 10, no. 1, p. 6007, Apr. 2020.

Hanyue Shangguan (Graduate Student Member, IEEE) received the bachelor's degree in material science engineering from the University of Toronto, Toronto, ON, Canada, in 2016. He is currently pursuing the Ph.D. degree in electrical and computer engineering with the University of Waterloo, Waterloo, ON, Canada.

He is a member of the Laboratory on Innovative Technology in Medical Ultrasound (LITMUS) at the University of Waterloo. His current research interests include the design of contrast agents, microvascular phantoms, and molecular ultrasound imaging techniques.

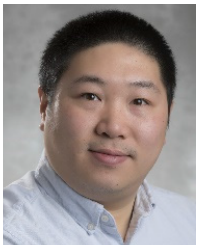

Billy Y. S. Yiu (Member, IEEE) received the B.Eng. degree (Hons.) in medical engineering and the M.Phil. degree in electrical and electronic engineering from the University of Hong Kong, Hong Kong, in 2007 and 2010, respectively, and the Ph.D. degree in electrical and computer engineering from the University of Waterloo, Waterloo, ON, Canada, in 2019.

Before joining the University of Waterloo, he was a Research Staff at the Biomedical Ultrasound Laboratory, University of Hong Kong. From 2021 to 2023, he was a Research Assistant Professor and the Co-Principal Investigator of LITMUS at the University of Waterloo. In 2023, he joined the Technical University of Denmark, Kongens Lyngby, Denmark, as an Associate Professor. He is also the Co-Instructor for the "Ultrasound Signal Processing with GPUs" short course at the IEEE Ultrasonics Symposium. His research interests are in advanced ultrasound imaging techniques and systems.

Dr. Yiu was a past recipient of the USE Young Scientist Award, the KSUM Young Investigator Gold Prize Award, and the ASA Biomedical Acoustics Best Student Paper Award.

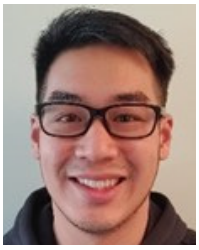

Adrian J. Y. Chee (Member, IEEE) received the B.Eng. degree in electrical and computer systems engineering from Monash University, Melbourne, Australia, in 2011, and the Ph.D. degree in mechanical engineering from the University of Hong Kong, Hong Kong, in 2016.

He was a Corporate Intern at Hitachi Central Research Laboratory, Tokyo, Japan, in 2016. He is now an Associate Scientist with the Laboratory on Innovative Technology in Medical Ultrasound, University of Waterloo, ON, Canada. His research interests include designing new vascular ultrasound techniques and related experimental tools.

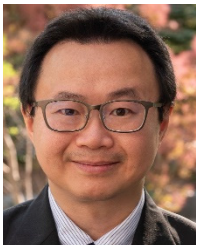

Alfred C. H. Yu (Fellow, IEEE) received the B.Sc. degree in electrical engineering from the University of Calgary, Calgary, AB, Canada, in 2002, and the M.A.Sc. and Ph.D. degrees in biomedical engineering from the University of Toronto, Toronto, ON, Canada, in 2004 and 2007, respectively.

From 2007 to 2015, he was the Founding Principal Investigator of the Biomedical Ultrasound Laboratory, University of Hong Kong, Hong Kong. In 2015, he relocated to the University of Waterloo, Waterloo, ON, Canada, where he is currently the Assistant Vice-President, Research and International and Professor in Biomedical Engineering. He has long-standing research interests include ultrasound imaging and therapeutics.

Dr. Yu is an NSERC Steacie Memorial Fellow. He is also a fellow of the American Institute of Ultrasound in Medicine (AIUM), the Canadian Academy of Engineering (CAE), and the Engineering Institute of Canada (EIC). Earlier in his career, he was a recipient of the IEEE Ultrasonics Early Career Investigator Award, the Frederic Lizzi Award, and the Ontario Early Researcher Award. He was previously the Program Chair of 2023 IEEE Ultrasonics Symposium, the Chair of the Medical Ultrasound Group of the IEEE Ultrasonics Symposium, and an Elected AdCom Member of the IEEE UFFC Society. He is now the Editor-in-Chief of IEEE TRANSACTIONS ON ULTRASONICS, FERROELECTRICS, AND FREQUENCY CONTROL.